2024 IEEE International Conference on Communications Workshops (ICC Workshops) | 979-8-3503-0405-3/24/$31.00 ©2024 IEEE | DOI: 10.1109/ICCWORKSHOPS59551.2024.10615381

Downlink-Uplink Symmetry in Mobile Battery-Free Retro-Reflective VLC: Enabling Sensing-Assisted Communications

Sihua Shao*, Adrian Salustri*, Alexander Heusser*, Hassan Khaniani†, Mostafa Hassanalian‡, Pedram Roghanchi§

*Department of Electrical Engineering, New Mexico Tech, Socorro, NM 87801. Email: sihua.shao@nmt.edu

†PRRC, New Mexico Tech, Socorro, NM 87801. Email: hassan.khaniani@nmt.edu

‡Department of Mechanical Engineering, New Mexico Tech, Socorro, NM 87801. Email: mostafa.hassanalian@nmt.edu

§Department of Mining Engineering, University of Kentucky, Lexington, KY 40508. Email: pedram.roghanchi@uky.edu

***Abstract*—Designing a mobile retro-reflective visible light communication (R-VLC) system presents significant challenges due to the rapid and substantial changes in uplink channel gain. These changes occur when the retro-reflective tag, crucial for the system's operation, is worn by a person in motion. Consider a scenario where an intelligent rescue drone is leading the assisted-escape for miners trapped due to an accident. The drone, equipped with a searchlight, facilitates duplex communication with the trapped miners via a batteryless R-VLC system. Despite the retro-reflective tag's unique ability to support self-alignment in the VLC system, the tag's orientation changes quickly as a miner moves. This movement induces significant variations in the uplink channel gain, which requires a fast adaptive modulation and coding scheme. In response to this challenge, our work involves prototyping an R-VLC system powered by photovoltaic cells. Based on Manchester-coded on-off keying, the communication distance achieves up to 6 meters. Through channel characterization and experimental validation, we demonstrate that the prototype can leverage the downlink photovoltaic cell sensing output to directly estimate the strength of the uplink retro-reflected signal. The symmetry between downlink and uplink allows for symbol-wise adaptation, crucial for effective sensing-assisted communication.**

***Index Terms*—Sensing-assisted communication, battery-free, mobility, visible light communication, backscatter communication, drone-assisted mine rescue.**

I. Introduction

Deploying intelligent drones during mine rescue missions to locate and assist trapped miners in self-escaping substantially mitigates the risks to rescue teams navigating hard-to-reach areas within post-disaster underground mines. Establishing a consistent and dependable wireless communication link between drones and miners is crucial. This link allows the sophisticated rescue system to garner instructive feedback from miners engaged in self-escape efforts — for instance, communicating their distress level. Such feedback is essential, aiding rescue teams in comprehensively understanding and promptly responding to the unique needs and demands of trapped miners. In this scenario, battery-free, retro-reflective visible light communication (R-VLC) [1]–[5] emerges as a candidate to facilitate robust wireless communication.

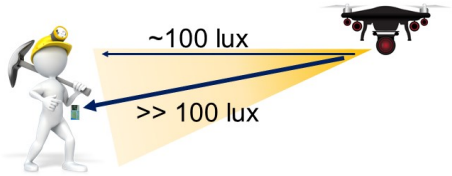

Fig. 1: Trapped miner uses the battery-free R-VLC tag to communicate with a intelligent rescue drone.

As depicted in Fig. 1, the rescue drone is equipped with a searchlight directed towards the miner. To maintain the searchlight within the miner's line of sight during self-escape, a lightweight acquisition, tracking, and pointing (ATP) system [6] could be utilized by the drone. This system dynamically adjusts both the beam orientation and the semi-angle at half power [7], [8], ensuring that the miner perceives adequate illuminance (e.g., 100 lux) and that a strong beam is cast towards the retro-reflective tag. The R-VLC, serving as an ultra-low power solution, offers several advantageous features: 1) it repurposes the searchlight for both power and communication; 2) it remains resilient against electromagnetic interference (EMI) from various radio devices; 3) it can be easily extend to support multiple access by using CMOS camera as the optical receiver; and 4) it guarantees precise transmitter-receiver alignment due to its retro-reflective nature. The comprehensive R-VLC system incorporates a light reader as well as one or more retro-reflective tags.

The light reader equipped on the drone is operational through the utilization of the LiFi technology [9]. R-VLC technology applying backscatter communication in optical domain was first introduced in 2015 [10]. The R-VLC system employs a retroreflector designed to redirect incident light back to its source with minimal scattering. This retroreflector can be crafted either from a corner-cube comprising three mutually

Corresponding author: Sihua Shao, sihua.shao@nmt.edu.

The work is supported by National Science Foundation (NSF) CNS-2245747 and National Institute for Occupational Safety & Health (NIOSH) U60 OH012351-01.

perpendicular reflective surfaces or from sheeting materials like those found in 3M Scotchlite reflective fabric [11]. When compared to the sheeting material, a corner-cube retroreflector experiences reduced scattering effects and more effectively concentrates the reflected light back to its original source. The R-VLC system proposes the use of a low-cost, low-SWaP (Size, Weight, and Power), ultra-low-power optical modulator with kHz-bandwidth, specifically an LCD shutter [12], to modulate the reflected optical signal. The LCD shutter functions by alternating between pass and block states, achieved through the application of an electric field to the liquid crystal layer.

Some literature refers to R-VLC as visible light backscatter (VLB) because of its reflection-based signal generation mechanism. A pixelated VLB was prototyped in [13] to support multilevel backscattered signals. Authors in [14]–[16] suggested encoding data on mobile surfaces using various reflecting materials. The study in [17] introduced trend-based modulation and code-assisted demodulation to enhance the data rate of on-off keying-based VLB uplinks to 1 kbps. Geometric analysis was used in [1]–[3] to derive the retroreflection loss of circular corner-cube retroreflectors. In [18], a detailed analysis of VLB system physical layer design was provided, showcasing a prototype employing frequency shift keying. The research in [19] separated two polarizers of an LCD shutter and implemented polarization-based differential reception to facilitate long-range VLB communication between vehicles and road signs. The study outlined in [20] developed delayed superimposition modulation (DSM) to leverage the rapid rising time of LCD shutters. It also integrated DSM with polarization-based QAM by extending DSM symbols to the I-Q plane. Focus was given to the birefringence values and liquid crystal thicknesses in [21] to improve switching speeds without significantly compromising the contrast ratio. Most recently, [22] explored the use of another optical modulator, the digital micro-mirror device, which exchanged milliwatt power consumption for a tenfold increase in data rate. *Despite a decade of advancements in R-VLC technology, none of the existing studies have considered the challenges posed by irregular wearable tag orientation variations resulting from human movement.*

In this paper, we initiate our examination by exploring the battery-free capability of utilizing a well-developed amorphous silicon solar cell. This cell powers both the LCD shutter and the driver circuits, as discussed in Sec. II. A MOSFET is employed to switch between sensing and power supply functions. Upon validating the communication performance over a considerable distance (Sec. IV-A), we proceed to characterize the solar cell output V_{s} and the retro-reflected signal strength V_{r}. We demonstrate the linear relationship between these two variables in Sec. III. Measurements of V_{s} and V_{r} are taken at varying communication distances and tag orientations, as outlined in Sec. IV-B. The obtained results suggest that V_{s} can serve as an accurate estimator for V_{r}, provided that the incidence angle to the tag is known. It is worth noticing that the findings of this study not only have implications for the research at

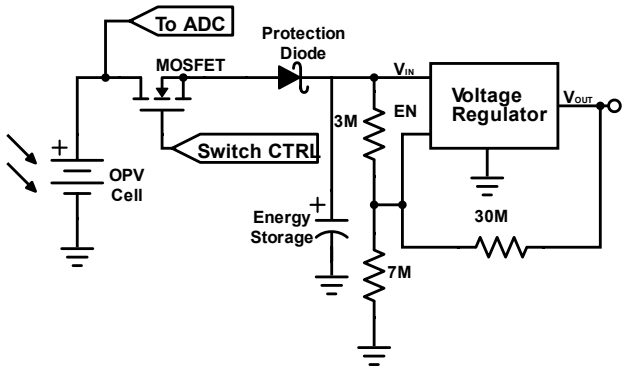

Fig. 2: A diagram illustrating the photovoltaic cell based power supply circuit design. The MOSFET is used to switch between sensing mode and power supply mode.

hand but also are valuable for enhancing communication and tracking in wearable devices across various applications. This is especially significant in domains where electromagnetic interference (EMI) poses substantial challenges, evident in fields like smart healthcare and intelligent manufacturing, particularly in scenarios involving human-computer interaction.

The contributions of our work are summarized below:

- We introduce a battery-free design that simultaneously supports photovoltaic sensing and powering.
- Channel characterization proves a linear relationship between uplink signal strength and downlink sensing value.
- Through tunnel experiments, we validate the practical communication distance achievable with our design.
- Comprehensive experimentation showcases the feasibility of utilizing the output from photovoltaic sensing to accurately estimate the strength of the retro-reflected signal.

II. Battery-Free Design

The battery-free design is comprised of two primary modules: the power harvesting module and the sensing/charging switch module, as illustrated in Fig. 2. The power harvesting module employs a photovoltaic (PV) cell—such as an amorphous silicon solar cell or an organic photovoltaic cell—to convert the optical power of the incident searchlight into electrical power. Our evaluation encompasses two distinct types of PV cells: the amorphous silicon solar cell [23] and the organic PV (OPV) cell [24]. Generally, we found that the silicon PV cell boasts superior energy efficiency compared to the OPV cell. However, when the incident illuminance is relatively low (e.g., $<$100 lux), the output voltage of the silicon PV cell swiftly diminishes to zero, whereas the OPV cell continues to maintain a stable voltage output. Furthermore, the inkjet printed free-shape feature of the OPV cell is advantageous as it allows the energy harvesting unit to optimally utilize the available area in specific application scenarios.

In the design [25], a low forward bias Schottky diode is cascaded with the PV cell, serving to protect the cell from reverse current discharge. A large capacitor (e.g., 68 μF) is incorporated to both store harvested energy and stabilize the

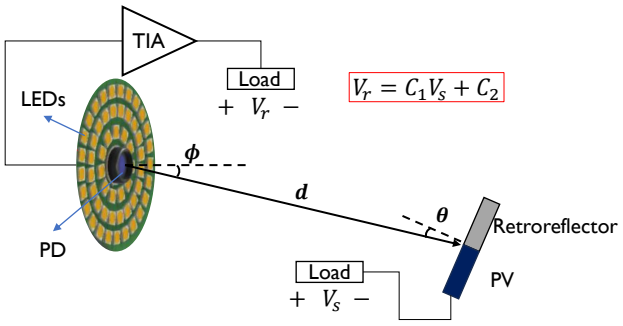

Fig. 3: A diagram illustrating the DC voltage outputs and the relative location and orientation of the light reader and the retro-reflective tag.

current flowing into the voltage regulator. Note that increasing the capacitor's capacitance will extend the cold start time (the initial energy collection period required by the driver circuit before startup), whereas decreasing the capacitance will lead to a rapid drop in V_{IN} if PV cell provides inadequate power.

To ensure a stable supply voltage V_{OUT} for the microcontroller unit (MCU), a low drop-out linear voltage regulator is utilized. The Enable pin feature, coupled with a feedback network for hysteresis, is used. We use the Enable pin feature and a feedback network to provide hysteresis. This approach stabilizes V_{OUT} by establishing different ON and OFF voltage values, contingent on MCU's operational supply voltage range. Compared to other R-VLC battery-free designs [10], [17], the design presented in Fig. 2 notably simplifies the circuitry while maintaining data transmission capability under low light levels.

To measure the sensing output from the PV cell, it is required to intermittently disconnect the PV cell from the charging circuit. This disconnection is facilitated by a MOSFET, with its base governed by the MCU. When the MOSFET functions in the cutoff region, the PV cell is linked to the analog-to-digital converter (ADC). The ADC is responsible for sampling the analog output emitted by the PV cell, subsequently generating the sensing output. Due to its rapid switching speed and minimal power consumption, a MOSFET enables a smooth transition between the sensing and charging modes, incurring negligible energy overhead in the process.

III. Channel Characterization

In this section, we elucidate the characterization of the downlink and uplink channels existing between the light reader and the retro-reflector tag, subsequently establishing the linear relationship binding the two. As depicted in Fig. 3, due to the inherent property of retro-reflection, both the radiance angle emanating from the light reader and the incidence angle approaching the light reader are denoted as ϕ. Meanwhile, the incidence angle towards the retro-reflective tag is represented by θ. The signal that is retro-reflected (constituting the uplink) undergoes amplification by the transimpedance amplifier (TIA) and is subsequently characterized by the voltage measured across the load resistor. Correspondingly, the output yielded by the PV cell is defined by the voltage existing across the direct load resistor.

Proposition 1: With ϕ and θ held at constant values, the relationship between the DC voltage output from the photodetector (PD), denoted as V_{r}, and the DC voltage output from the PV cell, denoted as V_{s}, is linear under typical operational light conditions for the PV cell. This linear relationship can be mathematically articulated as follows:

$$V_{\text{r}} = C_1 V_{\text{s}} + C_2, \tag{1}$$

In this equation, C_1 and C_2 are constants.

Proof: To prove the Proposition 1, we commence by evaluating the optical powers received by the photodector and the PV cell, represented by P_{PD} and P_{PV}, respectively. Under the assumption that the transmitter produces an axially symmetric radiation pattern characterized by the radiant intensity (W/sr) $P_{\text{t}} R_{\text{o}}(\phi)$, the optical power received at the photodetector (PD) within its field-of-view (FOV) can be determined using the channel DC gain, as stated in [7], [8]. The uplink path loss model can be delineated by the following equation:

$$P_{\text{PD}} = P_{\text{t}} \frac{A_{\text{PD}}}{(2d)^2} R_{\text{o}}(\phi) T_{\text{s}}(\phi) g(\phi) \cos\phi \delta(\phi, \theta). \tag{2}$$

Here, A_{PD} refers to the physical area of the detector, and $R_{\text{o}}(\phi)$ is normalized such that $2\pi \int_0^{\pi} R_{\text{o}}(\phi) \sin\phi \; d\phi = 1$. Additionally, $T_{\text{s}}(\phi)$ denotes the filter's signal transmission, while $g(\phi)$ represents the concentrator gain. Owing to the retro-reflection property, the actual signal propagation distance is double the communication distance, represented as $2d$. The angle of incidence with respect to the receiver (PD) axis is equal to the angle of irradiance, leading to an effective signal collection area of $A_{\text{PD}} \cos\phi$. An additional loss factor is introduced as $\delta(\phi, \theta)$ (where $0 \leq \delta \leq 1$) which is influenced by the retro-reflective tag's position and orientation relative to the light reader. This factor, δ, quantifies the fraction of incident light reflected back towards the PD. In our prior research [5], the loss factor $\delta(\phi, \theta)$ was examined and characterized specifically for a corner-cube retro-reflector, revealing that δ remains unaffected by variations in d.

Characterizing the downlink channel is relatively straightforward since the PV cell can be conceptualized as a planar photodiode operating in photovoltaic mode. The optical power that the PV cell receives can be estimated using the equation

$$P_{\text{PV}} = P_{\text{t}} \frac{A_{\text{PV}}}{d^2} R_{\text{o}}(\phi) \cos\theta. \tag{3}$$

Given P_{PD}, the strength of the retro-reflected signal V_{r} can be represented as

$$V_{\text{r}} = P_{\text{PD}} \times E_{\text{OE}}^{\text{PD}} \times G_{\text{TIA}}. \tag{4}$$

Similarly, with P_{PV}, the sensing output from the PV cell V_{s} is given by

$$V_{\text{s}} = P_{\text{PV}} \times E_{\text{OE}}^{\text{PV}} \times R_{\text{L}} + K. \tag{5}$$

In these two equations, $E_{\text{OE}}^{\text{PD}}$ and $E_{\text{OE}}^{\text{PV}}$ denote the optical to electrical conversion efficiency factors for the PD and PV cell,

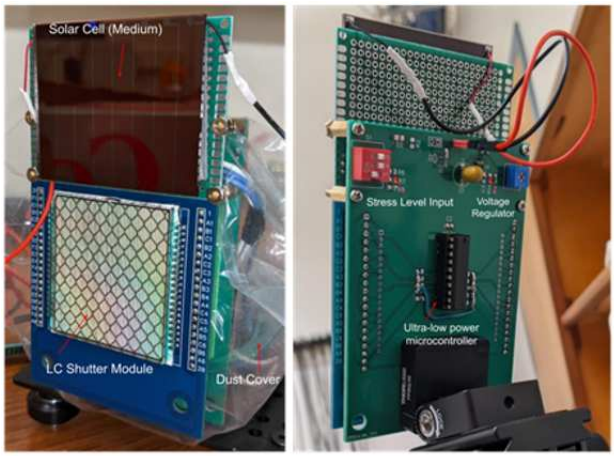

Fig. 4: Amorphous silicon solar cell powered R-VLC tag.

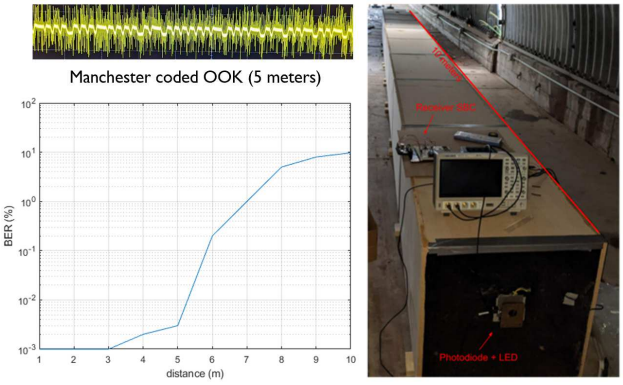

Fig. 5: Bit error rate performance using 100 Hz OOK signal.

respectively. G_{TIA} represents gain of the TIA, while R_{L} is the load resistance inherent to the PV cell circuit. The constant K is introduced to account for the non-linear relationship between the generated photocurrent from the PV cell and P_{PV} when P_{PV} approaches to zero.

Combining equations (2) - (5), we can conclude that

$$V_{\text{r}} = C_1 V_{\text{s}} + C_2, \tag{6}$$

where

$$C_1 = \frac{A_{\text{PD}} T_{\text{s}}(\phi) g(\phi) \cos\phi \delta(\phi,\theta) E_{\text{OE}}^{\text{PD}} G_{\text{TIA}}}{4 A_{\text{PV}} \cos\theta E_{\text{OE}}^{\text{PV}} R_{\text{L}}} \tag{7}$$

$$C_2 = -K C_1 \tag{8}$$

■

IV. Experiments

In this section, our initial evaluation focuses on determining the effective communication distance within an emulated tunnel environment, relying on the proposed battery-free design. Subsequently, we empirically validate the linear relationship between V_{r} and V_{s} by conducting measurements at various angles and distances.

A. Light Reader and Retro-reflective Tag

The initial experiment is geared towards evaluating the capacity of the uplink, which extends from the tag to the reader. The light reader is comprised of 16 XHP35 high-power LED modules, each powered by a 12V DC voltage source. This source is connected through a 4Ω resistor that acts as a current limiter. Positioned at the center of these LEDs is the embedded PD, specifically a silicon switchable gain detector (PD100A2) from Thorlabs, with its gain preset to 20 dB. The PD is mounted with a 25 mm focal length lens in a 1 inch diameter and 15 mm long lens tube. The PD's large active sensing area (75.4 mm^2) ensures the complete capture of the reflected optical signal after lens focusing. The PD output is connected to a Tektronix MDO4034C oscilloscope with 50 Ohm internal impedance. The output of the PD is fed directly into the oscilloscope with 2000 samples per second. The recorded samples of the modulated signal is exported to MATLAB for offline processing.

The retro-reflective tag is shown in Fig. 4. It consists of a retro-reflector made of 3M retro-reflective tape covered by a 50 mm x 50 mm graphic shutter from Liquid Crystal Technologies [12]. The graphic LCD shutter consists of 36 pixel, each of which is 6 mm x 6mm. The PV cell is an amorphous silicon solar cell with three different sizes: 1) 5 cm x 2.5 cm; 2) 6 cm x 5 cm; 3) 10 cm x 5.5 cm. The energy harvesting circuit is implemented based on the circuit diagram presented in Fig. 2. MCU M430G2553 is utilized to manipulate the graphic LCD shutter. Each I/O pin on the MCU transmits a TTL logic signal, managing its associated pixel with independent timing. For the purposes of this experiment, the retro-reflected signal, pre-coded within the MCU, is transmitted as soon as the MCU's supply voltage enters the operational range.

As shown in Fig. 5, we assembled a dust chamber to simulate an underground tunnel environment. The light reader was mounted on one end of the chamber, while the retro-reflected tag was situated at varying distances within the chamber. Measurements began with the control computer activating the light reader, initiating the sampling of the PD output signal, and storing the resultant data. Each distance setting involved a 40-second recording period, after which the data was transferred to a host computer for decoding purposes. The retro-reflected signal employed was a self-clocking Manchester-coded on-off keying (OOK) signal operating at 100 Hz. We assessed the bit error rate (BER) at distances ranging from 1 meter to 10 meters. As indicated in Fig. 5, the BER remains below 0.5% up to 6 meters and stays under 10% at a distance of 10 meters. The tag is capable of initiating operations with incident light levels below 100 Lux, albeit with an extended cold start time. Table I provides a summary of the effects of the solar panel and ambient light levels on cold start time.

B. Experimental Validation for Proposition 1

Having validated the battery-free design and assessed the communication distance, the second experiment is designed to measure V_{r} and V_{s}, as defined in Proposition 1, at various

TABLE I: Cold start time

PV cell size (cm)	100 Lux	500 Lux
5 x 2.5	9.35 s	2.89 s
6 x 5	6.97 s	1.20 s
10 x 5.5	2.94 s	.518 s

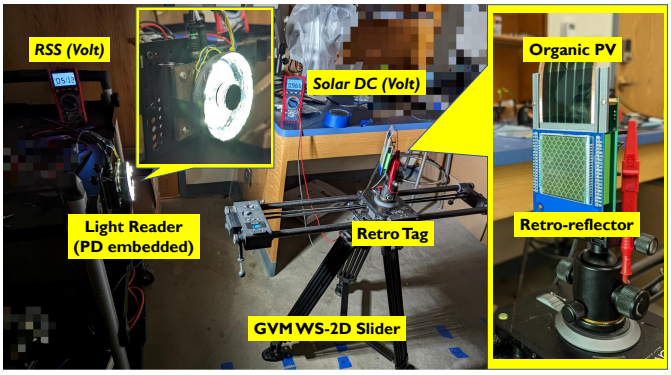

Fig. 6: Testbed for measuring V_r and V_s

distances and angles. In this setup (Fig. 6), we employed a 64 mm x 69 mm OPV cell [24]. The light reader was firmly fixed at a height identical to that of the retro-reflective tag. The tag itself was positioned on a GVM WS-2D slider, a device used for adjusting both the distance between the light reader and the tag as well as the incidence angle θ relative to the tag. A 4.7 kΩ load resistor was connected to the OPV cell output.

For the measurements, the tag was initially situated at the foremost position on the GVM slider, starting at a distance of 40 cm from the light reader. The GVM slider allows for 60 cm of movement. Fifteen distinct locations were identified at 4 cm intervals, ranging from 40 to 100 cm from the light reader, by utilizing two endpoints and fractional increments available in the GVM Slider app. The tag was then rotated on its vertical axis at each location to achieve five different incidence angles, ranging from 0 to 10 degrees in 2.5-degree increments. This process yielded a total of 75 unique combinations of location and angle. Three measurements were taken for each combination: first, the OPV DC output voltage V_s across the 4.7 kΩ load resistor; second, the received signal strength (RSS) at the PD; and third, the RSS at the PD with the retro-reflector obscured by opaque tape. The third measurement helped isolate noise and environmental reflections by being compared to the second measurement, thus extracting the retro-reflector's exclusive contribution to the RSS. The relationship between V_s and V_r was then plotted in Fig. 7a. Note that the angle-dependent attenuation of the LCD shutter is close to zero at small incidence angles. For larger incidence angles, additional calibrated attenuation factor $g(\theta)$ could be included in C_1.

In Fig. 7a, a linear regression model is employed to estimate the constants in the function $C_1V_s + C_2$. Notably, there is an observable deviation from the linear curve when the OPV DC voltage V_s exceeds 3V. This deviation primarily stems from OPV output saturation occurring as the OPV approaches closer to the light reader. To evaluate the impact of this deviation, measurements at $d = 40$ cm, as well as both $d = 40$ cm and $d = 44$ cm, are excluded; the resultant curve fittings are depicted in Fig. 7b and Fig. 7c, respectively. Interestingly, in Fig. 7a, when $\theta = 2.5°$, the value of $C_2 = -11$ exhibits opposite signage compared to the other four cases. This discrepancy is inconsistent with the analysis presented in Sec. III. According to Eq. 8, C_2 should consistently display either positive or negative signage, depending on that of K. However, in Fig. 7b and Fig. 7c, the C_2 value for the case of $\theta = 2.5°$ is estimated as -5.7 and -2.6, respectively, indicating a significant reduction in error. The residual errors for Fig. 7 are plotted in Fig. 8. Excluding measurements at $d = 40$ cm and $d = 44$ cm leads to a reduction in residual errors, decreasing from 3.15 mV to 1.5 mV.

V. Conclusion

The prototype of the battery-free R-VLC showcases the feasibility of utilizing a wearable device-sized tag to repurpose the searchlight for both power and communication over a

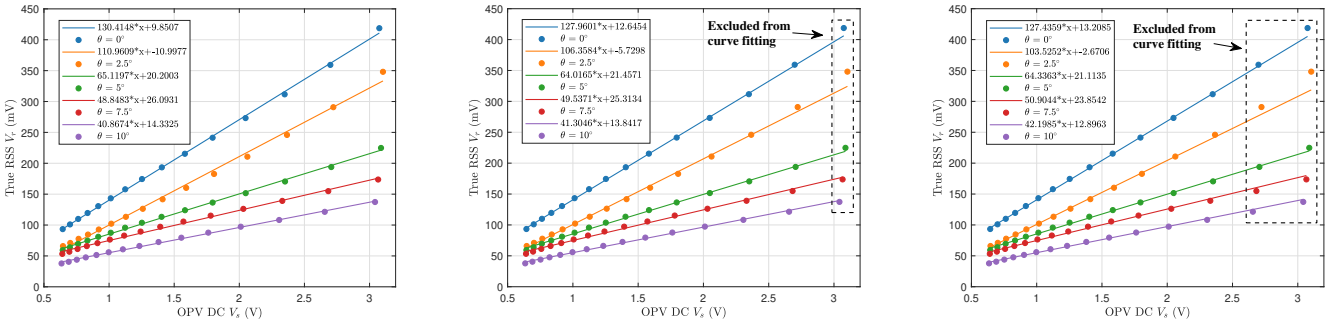

(a) No exclusion (b) Exclude $d = 40$ cm (c) Exclude $d = 40$ cm and $d = 44$ cm

Fig. 7: The scatter plot displays the relationship between the measured OPV DC output (V_s) and the true RSS (V_r) with data points represented by dots. Curve fitting results are depicted using solid lines. In subplot (a), all data points are included in the curve fitting process. In subplot (b), data points measured at a distance (d) of 40 cm are excluded from curve fitting. In subplot (c), data points measured at distances of 40 cm and 44 cm are excluded from curve fitting.

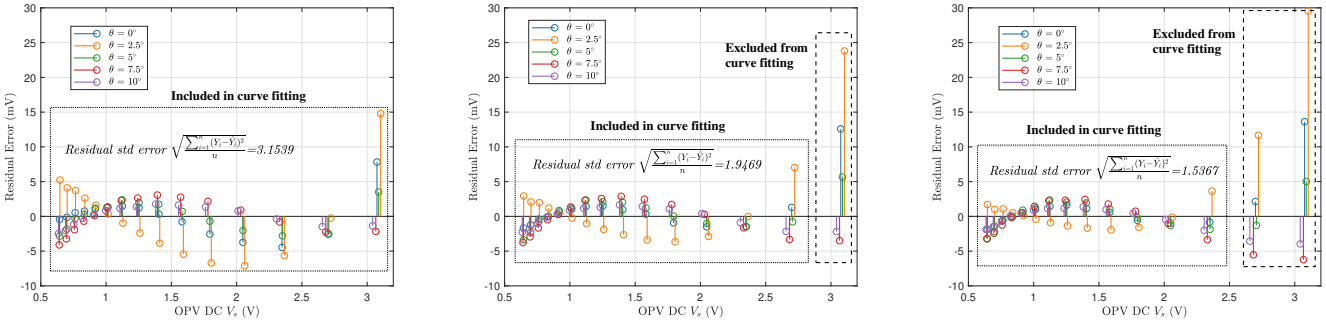

(a) Standard Error = 3.1539 mV (b) Standard Error = 1.9469 mV (c) Standard Error = 1.5367 mV

Fig. 8: Residual errors corresponding to Figs. 7 (a)-(c) are displayed respectively. The residual standard errors are computed based on the data points involved in the curve fitting process for each subplot.

reasonably long distance. Both theoretical analysis and experimental results substantiate the downlink-uplink symmetry property inherent to the R-VLC system. This property suggests that, provided the incidence angle θ is known, the strength of the retro-reflected signal can be accurately inferred from the PV cell sensing value. Consequently, without the need for explicit channel state information exchange, this sensing output can facilitate uplink modulation, e.g., adaptively change an OOK symbol length according to the sensing output to maintain the same average symbol energy at the reader side. Looking ahead, our future work will be dedicated to devising a low-power circuit to measure θ and developing a sensing-aided uplink modulation scheme.

REFERENCES

[1] S. Shao, A. Khreishah, and I. Khalil, "Retro: Retroreflector based visible light indoor localization for real-time tracking of iot devices," in *IEEE INFOCOM 2018-IEEE Conference on Computer Communications*. IEEE, 2018, pp. 1025–1033.

[2] ——, "Enabling real-time indoor tracking of iot devices through visible light retroreflection," *IEEE Transactions on Mobile Computing*, vol. 19, no. 4, pp. 836–851, 2019.

[3] S. Shao, A. Khreishah, and J. Paez, "Passiveretro: Enabling completely passive visible light localization for iot applications," in *IEEE INFOCOM 2019-IEEE Conference on Computer Communications*. IEEE, 2019, pp. 1540–1548.

[4] M. Salas, S. Shao, A. Salustri, Z. Schroeck, and J. Zheng, "Securing smart grid enabled home area networks with retro-reflective visible light communication," *Sensors*, vol. 23, no. 3, p. 1245, 2023.

[5] S. Shao, A. Salustri, A. Khreishah, C. Xu, and S. Ma, "R-vlcp: Channel modeling and simulation in retroreflective visible light communication and positioning systems," *IEEE Internet of Things Journal*, 2023.

[6] X. Sun, T. Zhang, S. Shao, B. Tice, P. Tice, and S. Jayaweera, "Low cost atp system design for free space optics based drone assisted wireless networks," in *2022 IEEE Globecom Workshops (GC Wkshps)*. IEEE, 2022, pp. 891–896.

[7] J. M. Kahn and J. R. Barry, "Wireless infrared communications," *Proceedings of the IEEE*, vol. 85, no. 2, pp. 265–298, 1997.

[8] T. Komine and M. Nakagawa, "Fundamental analysis for visible-light communication system using LED lights," *IEEE Transactions on Consumer Electronics*, vol. 50, no. 1, pp. 100–107, 2004.

[9] pureLiFi, https://purelifi.com/purelifi-pushes-connectivity-in-the-home-to-new-limits-with-lifihome/, 2022, [Online].

[10] J. Li, A. Liu, G. Shen, L. Li, C. Sun, and F. Zhao, "Retro-vlc: Enabling battery-free duplex visible light communication for mobile and iot applications," in *Proceedings of the 16th International Workshop on Mobile Computing Systems and Applications*, 2015, pp. 21–26.

[11] 3M, https://www.3m.com/3M/en_US/p/c/ppe/apparel/reflective-fabrics/i/safety/personal-safety/, [Online].

[12] Liquid Crystal Technologies, http://www.liquidcrystaltechnologies.com/, [Online].

[13] S. Shao, A. Khreishah, and H. Elgala, "Pixelated VLC-backscattering for self-charging indoor IoT devices," *IEEE Photonics Technology Letters*, vol. 29, no. 2, pp. 177–180, 2016.

[14] Q. Wang, M. Zuniga, and D. Giustiniano, "Passive communication with ambient light," in *Proceedings of the 12th ACM CoNEXT*, 2016, pp. 97–104.

[15] R. Bloom, M. Zuniga, Q. Wang, and D. Giustiniano, "Tweeting with sunlight: Encoding data on mobile objects," in *IEEE INFOCOM 2019-IEEE Conference on Computer Communications*. IEEE, 2019, pp. 1324–1332.

[16] W. Wang, Q. Wang, J. Zhang, and M. Zuniga, "Passivevlp: Leveraging smart lights for passive positioning," *ACM Transactions on Internet of Things*, vol. 1, no. 1, pp. 1–24, 2020.

[17] X. Xu, Y. Shen, J. Yang, C. Xu, G. Shen, G. Chen, and Y. Ni, "PassiveVLC: Enabling practical visible light backscatter communication for battery-free IoT applications," in *Proceedings of the 23rd Annual International Conference on Mobile Computing and Networking*, 2017, pp. 180–192.

[18] R. Bloom, M. Z. Zamalloa, and C. Pai, "Luxlink: creating a wireless link from ambient light," in *Proceedings of the 17th Conference on Embedded Networked Sensor Systems*, 2019, pp. 166–178.

[19] P. Wang, L. Feng, G. Chen, C. Xu, Y. Wu, K. Xu, G. Shen, K. Du, G. Huang, and X. Liu, "Renovating road signs for infrastructure-to-vehicle networking: a visible light backscatter communication and networking approach," in *Proceedings of the 26th Annual International Conference on Mobile Computing and Networking*, 2020, pp. 1–13.

[20] Y. Wu, P. Wang, K. Xu, L. Feng, and C. Xu, "Turboboosting visible light backscatter communication," in *Proceedings of the Annual conference of the ACM Special Interest Group on Data Communication on the applications, technologies, architectures, and protocols for computer communication*, 2020, pp. 186–197.

[21] S. K. Ghiasi, M. A. Z. Zamalloa, and K. Langendoen, "A principled design for passive light communication," in *Proceedings of the 27th Annual International Conference on Mobile Computing and Networking*, 2021, pp. 121–133.

[22] T. Xu, M. C. Tapia, and M. Zúñiga, "Exploiting digital Micro-Mirror devices for ambient light communication," in *19th USENIX Symposium on Networked Systems Design and Implementation (NSDI 22)*, 2022, pp. 387–400.

[23] Amorphous Silicon Solar Cell, https://www.mouser.com/datasheet/2/315/EP120B-775610.pdf, [Online].

[24] Organic Photovoltaic Cell, https://dracula-technologies.com/, [Online].

[25] V. Iyer, H. Gaensbauer, T. L. Daniel, and S. Gollakota, "Wind dispersal of battery-free wireless devices," *Nature*, vol. 603, no. 7901, pp. 427–433, 2022.